CHEMISTRY
A EUROPEAN JOURNAL

DOI: 10.1002/chem.200800992

One-Step Synthesis of Stoichiometrically Defined Metal Oxide Nanoparticles at Room Temperature

Lan Chen,[a] Ju Xu,[a] David A. Tanner,[b] Richard Phelan,[a] Machteld Van der Meulen,[a] Justin D. Holmes,[a] and Michael A. Morris*[a]

Abstract: A great variety of metal oxide nanoparticles have been readily synthesized by using alkali metal oxides, M_2O (M is Na or Li) and soluble metal salts (metal chlorides) in polar organic solutions, for example, methanol and ethanol, at room temperature. The oxidation states of the metals in the resulting metal oxides (Cu_2O, CuO, ZnO, Al_2O_3, Fe_2O_3, Bi_2O_3, TiO_2, SnO_2, CeO_2, Nb_2O_5, WO_3, and $CoFe_2O_4$) range from 1 to 6 and remain invariable through the reactions where good control of stoichiometry is achieved. Metal oxide nanoparticles are 1–30 nm and have good monodispersivity and displayed comparable optical spectra. These syntheses are based on a general ion reaction pathway during which the precipitate occurs when O^{2-} ions meet metal cations (M^{n+}) in anhydrous solution and the reaction equation is $M^{n+} + n/2\,O^{2-} \rightarrow MO_{n/2}$ ($n=1$–6).

Keywords: metal oxides · metathesis · nanoparticles

Introduction

Metal oxides play a very important role in many areas of chemistry, physics, and materials science.[1–6] The unique characteristics of metal oxides make them a very diverse class of materials, with properties covering almost all aspects of materials science and solid-state physics. Oxidic materials exhibit fascinating electronic and magnetic properties, including metallic, semiconducting, superconducting, or insulating and ferro-, ferri-, or antiferromagnetic behaviors.

In technological applications, oxides are used in the fabrication of microelectronic circuits,[7] capacitors,[8] sensors,[9] piezoelectric devices,[10] fuel cells,[11] semiconductors,[12,13] oxygen generators,[14] organic synthetics,[15–19] the manufacture of engineered ceramics,[20] coatings for the passivation of surfaces against corrosion,[21] and as catalysts as both the support and active component.[22–24] However, nanoscale metal oxides are particularly attractive to both pure and applied researchers because of the great variety of structure and properties, especially those related to intrinsic size-dependent properties.[11,24–27]

The preparation of metal oxide nanoparticles/nanocrystals with different sizes is important for the continued development of many fields of application, such as catalysis, photonic devices, electronic devices, and sensors, provided materials can be prepared at controlled size and reasonable cost. However, preparation of dimension-controlled oxide nanoparticles is difficult because of the unavoidable conglomeration trends of the nucleation and growth phase during hydrothermal, calcination, and condensation processes.

The precipitation of metal oxides from both aqueous and nonaqueous solutions is less straightforward than the precipitation of their metal sulfides or oxy salts. Reactions for the synthesis of metal oxides can generally be divided into two categories: those that produce an oxide directly[28–32] and those that produce what is best termed a precursor that must be subjected to further processing (calcination, dehydration, condensation, etc.).[33–38]

Most of the metal oxides can be prepared by precipitating the corresponding metal hydroxide, carbonate, oxalate, and even nitrate products, followed by their subsequent calcination, decomposition, or dehydration. High temperatures (calcination) or high pressures (hydrothermal treatment) are usually necessary for the reactions, and as such they are usu-

[a] Dr. L. Chen, Dr. J. Xu, R. Phelan, M. Van der Meulen, Dr. J. D. Holmes, Prof. M. A. Morris
Department of Chemistry, University College Cork
Cork (Ireland)
Fax: (+353) 21-490-4097
E-mail: m.morris@ucc.ie

[b] Dr. D. A. Tanner
Department of Manufacturing and Operations Engineering and Materials and Surface Science Institute
University of Limerick, Limerick (Ireland)

Supporting information for this article is available on the WWW under http://dx.doi.org/10.1002/chem.200800992.

ally high-energy processes and the stoichiometry is difficult to control. Among these synthetic routes, the most promising one is the soft-chemistry route,[34,36,37] especially nonaqueous sol–gel preparation, in which good control from the molecular precursor to the final product is achieved, offering high purity and homogeneity, and low processing temperatures (200–300 °C). In comparison to aqueous sol–gel chemistry, the synthesis of metal oxide materials in organic solvents under the exclusion of water provides some peculiar features, which allow better control over particle size, shape, crystallinity, and surface properties.[37] However, those syntheses mentioned above are neither direct nor simple routes due to the hydrolysis/condensation steps involved.

Combustion of metals in oxygen-containing air or electrolysis of metals in electrolyte solutions can produce corresponding oxides directly, but the process is also usually high-energy-consuming and incontrollable. Moreover, stoichiometric control is another challenge when the oxygen environment (concentration) varies on the surfaces of the oxides. A few successful examples of the direct synthesis of ZnO from organic solution at low temperature were reported,[32,39–43] for which expensive organometallic precursors were chosen as a Zn source and long reaction times were also necessary. However, the transfer of these procedures to other elements has not generally been proved.

Metal sulfides, for example, $MS_{n/2}$ can be made by $(NH_4)_2S$ or Na_2S reacting with soluble metal salts M_aX_b (M are metal ions and X designate chlorides, nitrates, sulfates, alkoxides and acetates, etc.) in aqueous solution at low temperature.[44–46] Can metal oxides be made in a similar way? To the best of our knowledge, no relevant experimental results have been reported todate. However, the reaction goes to completion providing that anhydrous polar solvents, such as methanol, ethanol, THF, acetone, formamide, and glycerol, are used instead of water, and that Na_2O is used instead of Na_2S in the above reaction.

In previous work we achieved the direct synthesis of monodispersed ZnO nanoparticles from $ZnCl_2$ in anhydrous alcohol and proposed the concept of "direct liquid phase participation (DLPP)".[47] Herein we extend this method to a great variety of metal oxide NPs/NCs that are also precipitated directly in anhydrous solution by the DLPP pathway at room temperature. The resulting products are confirmed to have controllable oxidation state/stoichiometry in all cases. The general process outlined herein is based on an ion reaction pathway during which the precipitate occurs when O^{2-} ions meet metal cations in the solution.

Results and Discussion

Almost all transition-metal precursors, including lanthanum salts, can form corresponding oxides by the DLPP strategy. In this work, different oxides were prepared for metals from transition-metal groups I_B, II_B, III_B, IV_B, V_B, VI_B, $VIII_B$, and main groups III_A, IV_A, and V_A; for example, Cu_2O, CuO, ZnO, Al_2O_3, Fe_2O_3, Bi_2O_3, TiO_2, SnO_2, CeO_2, Nb_2O_5, WO_3, and $CoFe_2O_4$.

M_2O-type oxides: Cu_2O nanoparticles (≈14 nm, calculated by using the Scherrer formula, see Table 1) were synthesized in methanol at room temperature, and the reaction time was as long as 50 h, the longest for all of the syntheses described herein. This was attributed to the low solubility of CuCl in methanol, and the reaction did not go to completion. Because of the long reaction periods Cu^I is slightly oxidized to Cu^{II} in air and forms $Cu(OH)_2$ during the reaction (Figure 1). X-ray photoelectron spectra display features typi-

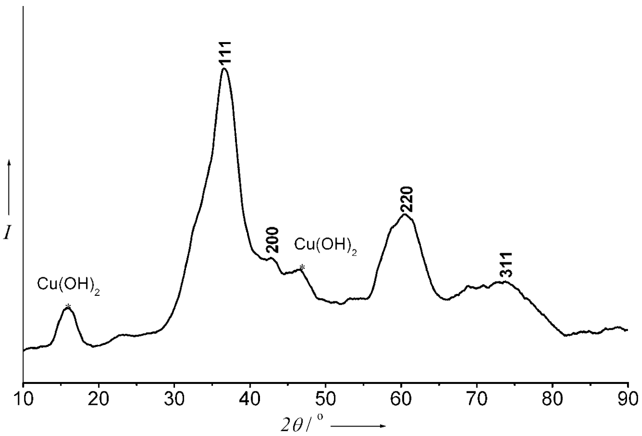

Figure 1. Powder X-ray diffraction pattern of M_2O-type nanoparticles (JCPDS 34–1354).

cal of univalent Cu 2p. This is characterized by the absence of satellite peaks at 940 and 945 eV (Figure 2).[48,49] The ratio of "Cu" to "O" stoichiometrically remains 1:2 as the formula is Cu_2O. Cu_2O is the only known binary *p*-type semiconducting oxide;[50] it possesses a direct band gap of 2.0 eV and a reasonably high room temperature hole mobility of about $100\,cm^2V^{-1}s^{-1}$. The UV/Vis absorbance spectrum (Figure 3) shows a sharp absorbance peak at 3.40 eV and a

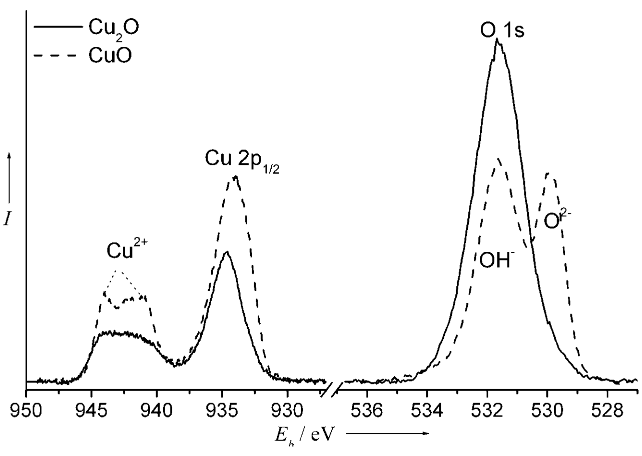

Figure 2. X-ray photoelectron spectra of uncapped copper oxides: two oxidation states (Cu^I, Cu^{II}) of Cu element.

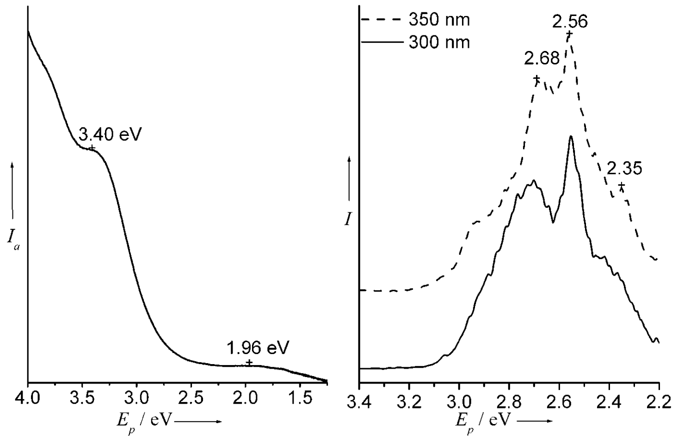

Figure 3. UV/Vis absorbance spectrum (left) and photoluminescence spectra of Cu_2O nanoparticles (right) at excitation wavelengths of 300 nm and 350 nm.

wide absorbance band at around 1.96 (1.98–2.17) eV. The peak at 3.40 eV is attributed to an energy level splitting in virtue of a quantum size effect of Cu_2O NPs, whereas the wide and flat bump at around 1.96 eV is the typical absorbance band of bulk Cu_2O.[50] The photoluminescence (PL) emission spectra at excitation wavelengths of 300 nm (4.13 eV) and 350 nm (3.54 eV) show two sets of similar emission features at 2.35, 2.56 and 2.68 eV respectively as shown in Figure 3. The size-dependent blue-shift of absorbance band gap of Cu_2O NPs was confirmed by these results.

MO-type oxides: TEM (Figure 4) shows typical precipitation examples of near monodispersed 0D oxide nanoparticles from alkali metal oxides. The examples shown are oleic acid-capped OLA-ZnO ($\approx$4.7 nm) and OLA-CuO ($\approx$3.6 nm) nanoparticles, respectively. The use of capping reagents, for example, 1-dodecylamine and oleic acid helps to make some oxide nanoparticles more uniform and monodispersed, for example, OLA-ZnO (see Figure S1a in the Supporting Information), whereas it makes little difference to other oxide nanoparticles, for example, OLA-CuO (see Figure S1b in the Supporting Information) in which the OLA-CuO nanoparticles tend to agglomerate together and form larger secondary particles of 10–20 nm (Figure 4, middle). Examples of stoichiometric control are further described in Figure 2 and 4, which show typical XPS data. For as-prepared copper samples (targeted as CuO) the Cu 2p peaks (Figure 2) around 934 eV have binding energies typical of the expected products.[48] The assignment is confirmed by the shape and intensity of the 2p satellite peaks around 942 eV.[48] The O1s features observed show that these surfaces are heavily hydroxylated with peaks at 529.8 (O^{2-}) and 531.7 (OH^-) eV. It is thought these are formed as a result of atmospheric exposure during the drying process at low temperature. Quantification of the Cu:O peak area ratio is consistent with the targeted stoichiometry. For the ZnO material (Figure 4, bottom), the Zn 2p3/2 feature (1021.8 eV) and O1 s features at 530.4 and 531.7 eV can be ascribed to Zn^{2+}, O^{2-}, and OH^-, and together with the Zn:O peak area ratio are consistent with the assignment of this material as ZnO. CuO and ZnO nanoparticles were synthesized with highly crystalline particles as confirmed by X-ray diffraction (Figure 5). ZnO normally has a hexagonal (wurtzite) crystal structure and is a direct band gap *n*-type semiconductor with $E_g = 3.25$ eV.[50] To illustrate the use of Li_2O as an O^{2-} source, wurtzite (ZnO) was prepared by this route whilst maintaining other experimental conditions. The photoluminescence spectra of ZnO in Figure 6 show four emission peaks between 2.54 and 3.21 eV (excited by 300 nm UV light). Similar peak positions were observed for both bulk and nanosized ZnO materials, and differences of emission intensity can be attributed to excitonic photoluminescence and mainly result from the relative quantities of surface oxygen vacancies and defects.[51] UV/Vis absorbance spectra of ZnO nanoparticles show an obvious blue-shift of absorbance band gap from 3.25 (bulk) to 3.56 eV (nanoparticles) due to the decrease in size of the ZnO materials. The band

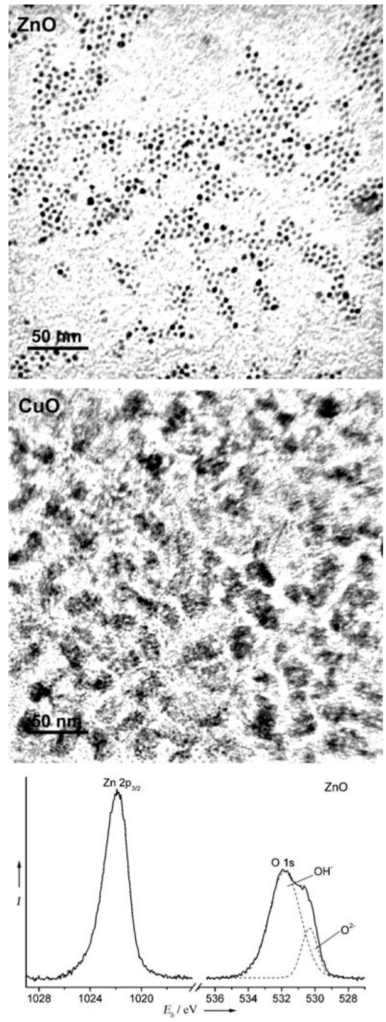

Figure 4. Transmission electron micrographs (TEMs) of oleic acid (top, middle) capped ZnO and CuO nanoparticles, and XPS profile of uncapped ZnO nanoparticles (bottom).

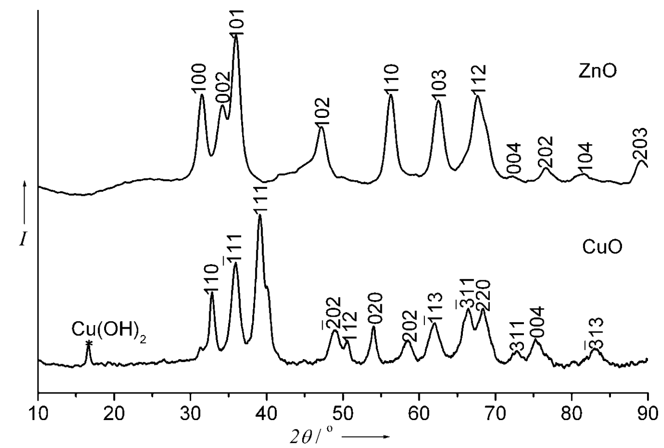

Figure 5. Powder X-ray diffraction patterns of MO-type nanoparticles (ZnO, JCPDS 36–1451; CuO, 05–0661).

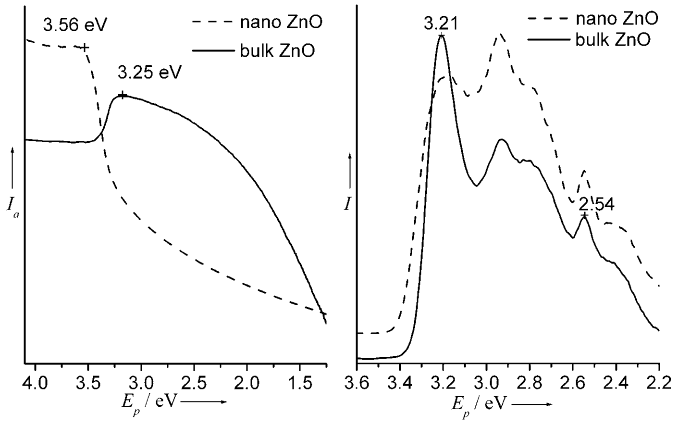

Figure 6. UV/Vis absorbance spectra (left) and photoluminescence spectra (right) at an excitation wavelength of 300 nm for both bulk ZnO and nanosized uncapped ZnO.

gap of ZnO nanparticles is 3.56 eV (Figure 6) and is typical of a wide-band semiconductor.[50,51]

Besides transition-metal oxides, II_A group oxides, for example, CaO and BaO can be obtained. However, the oxides are easily converted to the carbonates in air and it is therefore hard to obtain pure oxide materials under these experimental conditions. A mixture of two phases is usually obtained (oxides and carbonates). $Ca(OH)_2$ was formed as a product when laboratory methanol (the water content is less than 2 wt %) was used instead of anhydrous methanol. The sensitivity to water leading to hydroxide rather than oxide products has also been reported before.[52]

M_2O_3-type oxides: Crystalline Al_2O_3 and Bi_2O_3 are generally not easily synthesized at room temperature. TEM shows the formation of near monodisperse oleic acid capped Al_2O_3 nanoparticles with a diameter of 3.2 nm (Figure 7). X-ray diffraction data (Figure 8) show that both Al_2O_3 and Bi_2O_3 materials synthesized in this way display readily assignable X-ray diffraction peaks and the line broadening indicates

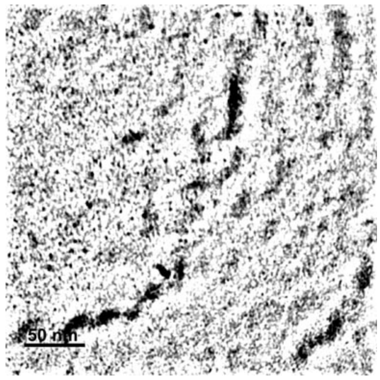

Figure 7. TEM image of oleic acid capped Al_2O_3 nanoparticles.

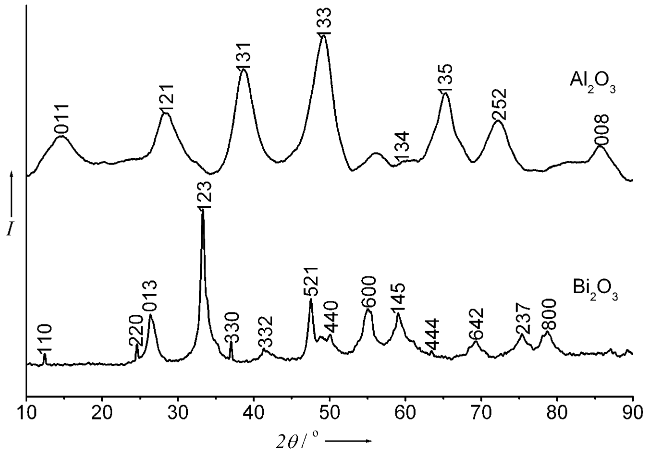

Figure 8. Powder X-ray diffraction patterns of M_2O_3-type nanoparticles (Al_2O_3, JCPDS 88–0107; Bi_2O_3, 74–1375).

that the nanoparticles are very small (as small as 3 nm in the case of Al_2O_3 and 12 nm for Bi_2O_3 nanoparticles). The X-ray photoelectron spectrum of the targeted Fe_2O_3 shows both Fe 2p and O 1s features and good indications of its stoichiometry (Figure 9). The Fe 2p3/2 peak at 711 eV is typical of Fe^{III}. The O 1s doublet shows resolved features at 530 (O^{2-}) and 531.7 (OH^-) eV that are typical of Fe_2O_3 exposed to air (water).[53]

Fe_2O_3 synthesized at room temperature is noncrystalline and requires high temperature to form a crystalline phase. However, it was found that crystalline Fe_2O_3 can be obtained in high boiling point solvents at 150 °C. The resulting material is magnetic and displays a strong attraction to a magnet. These results indicate that middle row transition elements (Fe, Co, and Ni) are difficult to make in crystalline form at room temperature, and elevated temperature is necessary for the formation of large crystal grains.

MO_2-type oxides: Figure 10 shows the formation of oleic acid capped monodispersed TiO_2 nanoparticles of about 3 nm, and CeO_2 and SnO_2 nanoparticles of about 4 nm observed by TEM. These are consistent with the X-ray diffraction peak broadening in Figure 8. X-ray photoelectron spec-

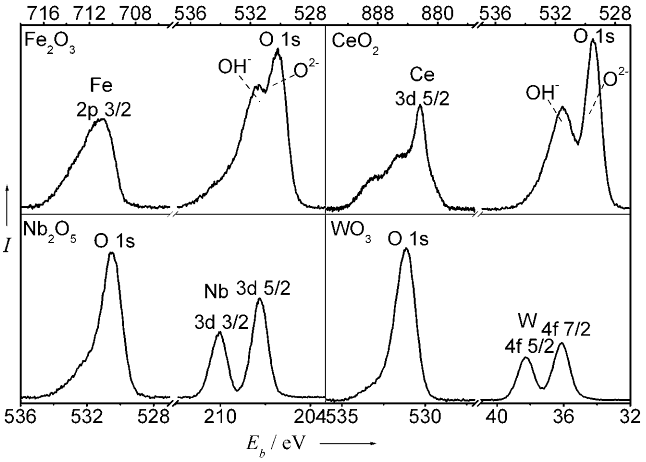

Figure 9. X-ray photoelectron spectra of metal oxides with higher oxidation state.

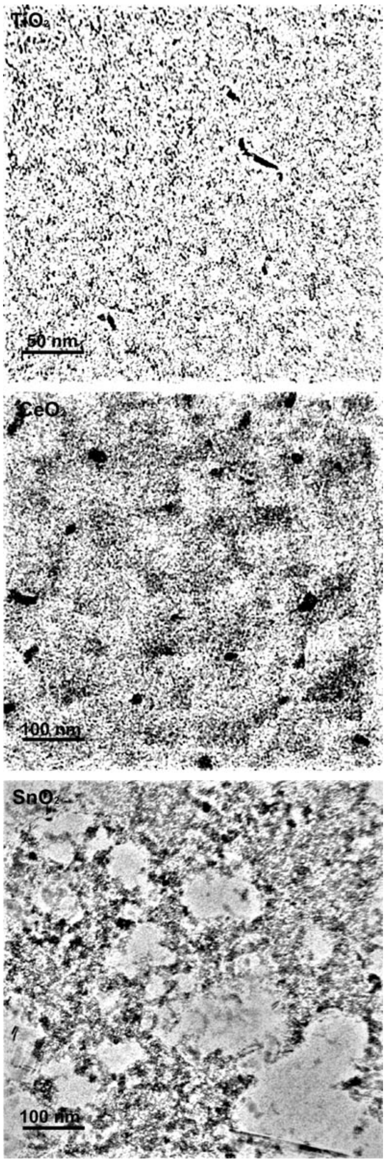

Figure 10. TEM image of oleic acid capped TiO_2 (top), uncapped CeO_2 (middle) and SnO_2 (bottom) nanoparticles.

troscopy (Figure 9, CeO_2) shows one sharp 3d5/2 peak at 882 eV and two smaller shoulders at 885 eV and 888 eV. These results are typical of Ce^{IV}.[54] The signals at 529 and 531 eV are assigned to O^{2-} and OH^- species, respectively. The water absorbed on the surface of CeO_2 nanoparticles is thought to arise from the washing process. Both SnO_2 and TiO_2 are direct band gap *n*-type semiconductors and have 3.6 and 3.0 eV band gaps, respectively. CeO_2 is used as a compound in the three-way catalyst for automotive exhausts.

Figure 11 shows that TiO_2, CeO_2, and SnO_2 all have well-resolved X-ray diffraction features and are small-sized particles (2–4 nm). SnO_2 and TiO_2 synthesized here were found

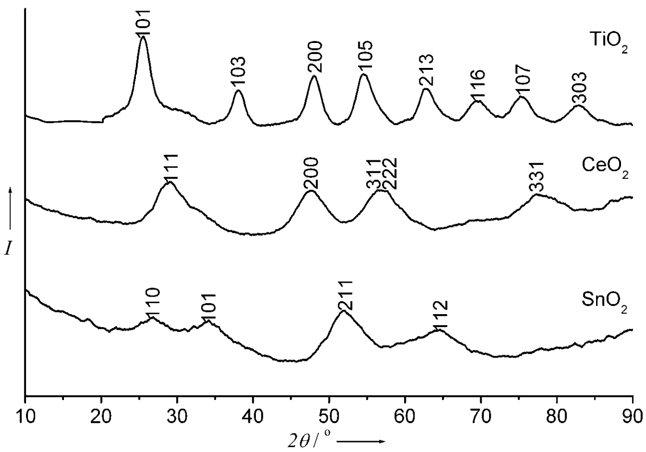

Figure 11. Powder X-ray diffraction patterns of MO_2-type nanoparticles (TiO_2, JCPDS 01–0562; CeO_2, 01–0800; SnO_2, 01–0625).

to exist as the cassiterite and anatase phase, respectively. Photoluminescence spectra of the MO_2 nanoparticles have three obvious emission peaks at around 2.5, 2.7, and 3.4 eV, respectively (at excitation lengths of 250 to 350 nm). Similar to that of ZnO nanoparticles, the photoluminescence of CeO_2 and TiO_2 can be attributed to the surface oxygen vacancies and defects (see Figure S2 in the Supporting Information). SnO_2 has lower intense photoluminescence reflections that indicate its wider band-gap in comparison to CeO_2 and TiO_2.

The UV/Vis absorbance spectrum (see Figure S3 in the Supporting Information) of CeO_2 nanoparticles shows an absorbance peak at 3.85 eV. This is significantly larger than any value previously reported[55] and can be attributed to a quantum size effect due to their small dimensions. The photoluminescence spectra of TiO_2 and SnO_2 nanoparticles are also shown in Figure S2 in the Supporting Information. The photoluminescence peaks of TiO_2 (at both 250 and 300 nm excitation) look similar to those of CeO_2 and probably relate to the similarity of their crystal structures.

A method developed by Kumar et al. is usually used to determine the band gap of semiconductor materials based on the measurement without obvious reflectance (absorbance) peaks as seen in Figure S3 in the Supporting Information.[56] By using this method we determined values of 3.95 (3.0) eV and 4.02 (3.6) eV for the direct band gap of TiO_2 and SnO_2 nanoparticles (see Figure S3 in the Supporting Information), respectively. These are much larger than the values (in parenthesis) of their corresponding bulk materials reported by Pearton et al.[50] It is reasonable to suggest that this is again attributable to quantum size effects.

M_2O_5-type and MO_3-type oxides: Figure 12 shows 2 nm sized WO_3 nanoparticles formed by this method. The broadening of the X-ray diffraction peaks (Figure 13) assigned to

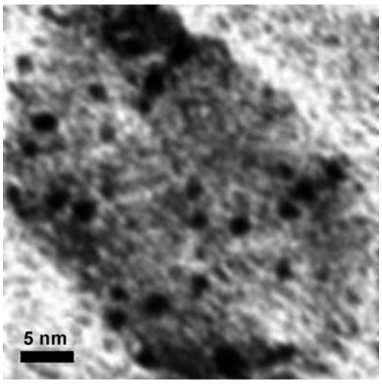

Figure 12. TEM image of uncapped WO_3 nanoparticles.

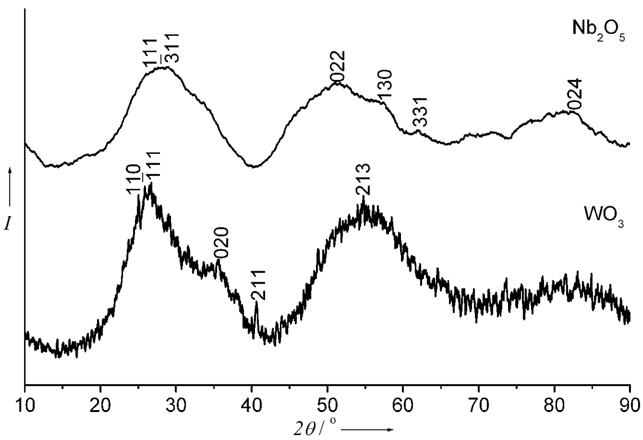

Figure 13. Powder X-ray diffraction pattern of M_2O_5-type (JCPDS 80–2493) and MO_3-type nanoparticles (JCPDS 88–0550).

Nb_2O_5 and WO_3 nanoparticles is consistent with the small sizes of the corresponding nanoparticles (1–2 nm). The X-ray photoelectron spectra of Nb_2O_5 and WO_3 have similar real shapes as shown in Figure 9. Binding energies at 207 eV and 210 eV are typical of Nb 3d5/2 and 3d3/2 peaks, respectively, and consistent with the targeted values. The intensity of the O 1s peak at 530 eV is about 2.5 times higher than that of the Nb 3d3/2 peak, which is assigned to Nb_2O_5. For WO_3, 4f7/2 and 4f5/2 peaks at 36 and 38 eV, respectively, are typical of the expected values for this oxidation state (W^{6+}) in oxides, and the intensity ratio of 3:1 for O 1s and W 4f 5/2 is also consistent with the stoichiometry of WO_3. The O1s peaks of both Nb_2O_5 and WO_3 show no splitting, which indicates that the surfaces are not readily hydroxylated as seen for other samples.

Ternary metal oxides: In addition to the binary metal oxides, ternary metal oxides can be synthesized by using the method described herein. One example is $CoFe_2O_4$ and Figure S4 in the Supporting Information shows the well-resolved crystalline structure obtained and the sharp diffraction peaks indicate the formation of nanocrystals. Low preparation temperatures, for example, room temperature do not result in the formation of any well-resolved crystalline structures even though $CoFe_2O_4$ can be co-precipitated by Co^{II} and Fe^{III} directly at such low temperatures. Elevating the temperature to annealing temperatures gives rise to transformation of the amorphous phase to the ordered phase that belongs to the JCPDS 03–0864 system, as confirmed by the X-ray diffraction and TEM data. TEM/electron diffraction data (see Figure S4 in the Supporting Information) shows Fe:Co = 2:1 in the high energy level and O:Fe + Co = 4:3 in the lower energy level, which are consistent with the formula of $CoFe_2O_4$. Such results show that the methodology can be used to carefully control the stoichiometry and hence the crystal phase in the structure-rich materials. A trace amount of Fe_2O_3 can be detected by X-ray diffraction, which is thought to be from a slight excess of Fe^{III} over Co^{II} ions in the system. The Cu signal is attributed to the copper grids used as the sample holder in TEM observation (see Figure S4 in the Supporting Information).

TEM data shows the formation of $CoFe_2O_4$ nanocrystals of the size 10–20 nm (Figure 14). The bright spots in the dark field image imply the formation of small particles with a well-developed crystalline wall. The electron diffraction pattern consists of seven clear multicrystalline rings that can exactly be assigned to the (111), (220), (311), (400), (422), (511), and (440) crystalline planes, respectively, for the JCPDS 03–0864 crystallographic system. Either the dark field image or the selected area electron diffraction (SAD) pattern confirms the materials are made of highly crystalline $CoFe_2O_4$ grains, that is, $CoFe_2O_4$ nanocrystals. However, the as-annealed $CoFe_2O_4$ sample also displays magnetic attraction to a magnet block.

DLPP mechanism: Clear solutions form when alkali metal oxide, for example, Na_2O (3 mmol) and metal chlorides (an equivalent amount) are completely dissolved in anhydrous methyl alcohol. In this solution, liquid-phase precipitation is thought to proceed as given in Equation (1):

$$MCl_n + n/2\,Na_2O \rightarrow n NaCl + MO_{n/2} \downarrow (n = 1-6) \quad (1)$$

In some nonaqueous solutions, this reaction is driven by the formation of either alkali metal halides or metal oxides. In our cases, a small amount of NaCl formed is totally dis-

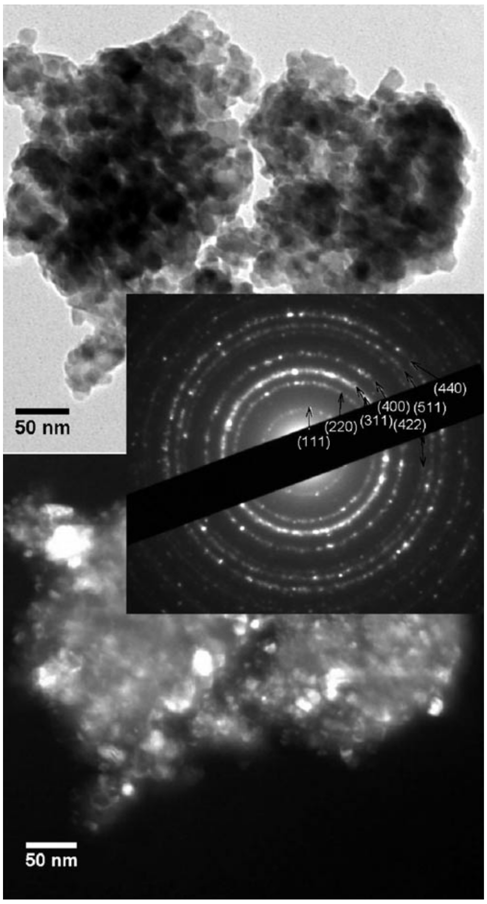

Figure 14. TEM (top) and dark field (bottom) images of $CoFe_2O_4$ NCs annealed at 500 °C for 10 h and its corresponding SAD pattern (inset).

Table 1. Synthesis conditions for metal oxides.

Oxides	Precursors	Solvents	Synthesis temperature [°C][a]	Reaction time [h][b]	Nanocrystal size [nm][c]
Cu_2O	CuCl	EtOH	RT (60)	2.5	– (14)
CeO_2	$(NH_4)_2Ce(NO_3)_6$	EtOH	RT (60)	4	4.2 (2.0)
TiO_2[d]	$TiCl_4$	MeOH	RT (60)	3	3.0 (4.1)
Nb_2O_5[d]	$NbCl_5$	MeOH	RT (60)	1	– (1.0)
WO_3	WCl_6	MeOH	RT (60)	3	2.0 (1.0)
Fe_2O_3	$FeCl_3$	MeOH	RT (60)	3	–
CuO	$CuCl_2$	EtOH	RT (60)	5	3.6 (4.8)
Al_2O_3	$AlCl_3$	MeOH	RT (60)	3	3.2 (2.9)
SnO_2	$SnCl_4$	EtOH	RT (60)	6.5	4.0 (2.1)
Bi_2O_3	$BiCl_3$	EtOH	RT (60)	3.5	– (13)
ZnO	$ZnCl_2$	MeOH	RT (60)	3	4.7 (5.9)
$CoFe_2O_4$	$CoCl_2$, $FeCl_3$	MeOH	RT (500)	29	15 (16)

[a] Room temperature (RT) is 19–28 °C and the value shown in parenthesis indicates the drying/annealing temperature. [b] Usually, products were aged for longer times than were needed for reaction completion. [c] Nanocrystal size was measured by TEM, and the data in parenthesis was estimated from X-ray diffraction data by using the Scherrer formula. [d] Precipitation did not start until the solvent volatilized and reached a certain concentration.

solved in a large quantity of ethanol and exists in the ion state in alcoholic (methanol or ethanol) solution. Thus, the reaction is only driven by the formation of thermodynamically stable metal oxide precipitates. In other words, the reaction, in fact, is completed as a simple ion reaction as shown in Equation (2):

$$M^{n+} + n/2\,O^{2-} \rightarrow MO_{n/2} \downarrow \ (n = 1-6) \quad (2)$$

Metal hydroxides can be formed if the solvents used are not strictly anhydrous or NaOH is used as the starting material instead of Na_2O and the hydroxides obtained under the conditions are (thermodynamic) stable enough to be detected by X-ray diffraction. The absence of hydroxides and other detectable precipitates under anhydrous conditions eliminates the possibility that the formation of the above oxides is derived from the decomposition of the intermediate products such as hydroxides and carbonates.

All experimental results as listed in Table 1 show that oxygen from solute molecules (e.g. Na_2O) rather than solvent molecules or ambient substances (O_2 or CO_2 in air) is the only oxide (O^{2-}) ion source, and the supposed intermediate products are not be formed under the present conditions. More detailed work is underway to explain this mechanism.

Conclusion

Metal oxides including the binary $MO_{n/2}$ ($n = 1$–6) oxides and the ternary $CoFe_2O_4$ oxide were synthesized by the DLPP strategy in a simple step at room temperature. Amongst them, Cu_2O, ZnO, TiO_2, SnO_2, and Nb_2O_5 are semiconducting oxides whose band properties and band gaps can be characterized by photoluminescence and UV/Vis absorbance spectra, whereas Fe_2O_3 and $CoFe_2O_4$ are magnetic oxides. As the only known binary *p*-type semiconducting oxide, Cu_2O was prepared from methanol solution and a blue-shift of its band gap by UV/Vis absorbance was observed. ZnO, SnO_2, and TiO_2, which are common wide-band semiconducting oxides, were made with band gaps of 3.56, 3.95, and 4.02 eV, respectively, due to the small sizes of the nanoparticles. In the case of ZnO nanoparticles, a blue-shift of absorbance band gap of 0.31 eV was obtained. Al_2O_3 and WO_3 particles, 2–3 nm in size, were directly precipitated in solutions. The addition of capping reagents, such as oleic acid makes the nanoparticles more uniform and monodispersed. In addition, 10–20 nm $CoFe_2O_4$ nanocrystals of strict stoichiometric ratio were also synthesized by using the strategy described herein, and the highly developed crystalline walls contribute the strong magnetic attraction.

Nanoparticles/nanocrystals of several nanometers were synthesized by using the general strategy at room temperature. Almost all metal oxide nanoparticles in the periodic table can be formed by this strategy. Ion precipitation makes it easy to synthesize small nanoparticles/nanocrystals. No calcination, no solvothermal treatment, and no electric field application (electrolysis) were required in the DLPP method. This makes it a unique method to synthesize metal oxide nanoparticles with the expected oxidation state of each element and the defined stoichiometry for each oxide. Lower dependence on equipment requirements combined with cheaper precursors (compared with organometallic syntheses under similar conditions) also makes this strategy a good candidate for the mass-production of metal oxide nanoparticles.

Experimental Section

Chemicals: Sodium oxide (97%), sodium peroxide (97%), and lithium oxide were purchased from Aldrich. Other reagent sources were defined below: CuCl, $ZnCl_2$, $BaCl_2$, $FeCl_3$, $BiCl_3$, $SnCl_4$, $(NH_4)_2Ce(NO_3)_6$, $NbCl_5$, WCl_6, 1-dodecylamine, oleic acid, methyl alcohol, ethyl alcohol, acetone, THF (Aldrich); $CuCl_2$ (BDH); $CaCl_2$ (Timstar Laboratory Suppliers); $MgCl_2$ (Alfa); $AlCl_3$, glycerol, chloroform (Riedel-de Haën); $TiCl_4$, octylamine, hexadecylamine, formamide (Fluka). All chemicals were either water-free as-received or following treatment under vacuum above the relevant dehydration temperature of the materials. Formamide and acetone were stored over dry 3 Å molecular sieves for three days prior to use, whereas THF, glycerol, methanol, ethanol, and chloroform were bought as anhydrous solvents.

Syntheses: In typical syntheses, anhydrous metal salts (3 mmol), for example, metal chlorides (MCl_n, $n=1$–6) were dissolved in anhydrous methanol (80 mL) to produce solutions 1. To accelerate the dissolution process, sonication in a bath (Cole-Parmer 8891) was sometimes performed. Following this, an equivalent amount of Na_2O was dissolved by sonication in another portion of anhydrous methanol (20 mL) to give solution 2. Solutions 1 and 2 were mixed under rigorous stirring for 1–12 h. All reactions were conducted in sealed vessels at room temperature. The resulting precipitates were aged in the mother liquor at room temperature for 12–36 h until complete precipitate separation occurred. To obtain monodispersed nanoparticles in some cases, alkylamines and oleic acid were added to solution 1 before the addition of solution 2; the molar ratio of metal cations to alkylamines and oleic acid was set at 1:1:0.5. The final products were collected by filtration using a filter paper (Whatman, grade 1) and washed several times with methanol and subsequently acetone for rapid drying. The wet products were dried at 60°C overnight.

Analyses: Powder X-ray diffraction (XRD) patterns were recorded on a Phillips Xpert MPD diffractometer by using $Cu_{K\alpha}$ radiation and a working voltage of 40 kV. Transmission electron micrographs (TEMs) were recorded on a JEM-2011 electron microscope operating at 200 kV. Oleic acid capped nanoparticles were dispersed into toluene before use and one or two drops of the above solution were placed on a holey carbon film on copper grids under dry ambient atmosphere at room temperature and left overnight. Powder X-ray photoelectron spectra (XPS) were recorded on a high performance AXIS 165 X-ray photoelectron spectrometer. Photoluminescence (PL) and UV/Vis absorbance spectra were obtained by using a Perkin Elmer LS50B fluorescence spectrometer and a Cary 50 UV-visible spectrophotometer, respectively. A small quantity of oxide nanoparticles (without capping reagents) was dispersed into ethanol, and solutions were placed in a quartz cell for optical analysis.

Acknowledgements

We thank the Science Foundation of Ireland (SFI, grant No. 03/IN3/I1375) for financial support, and Dr. Serguei Belochapkine, Materials and Surface Science Institute, University of Limerick for the XPS analysis.

[1] R. W. G. Wyckoff, *Inorganic compounds RX_n, R_nMX_2, R_nMX_3*, 2nd ed., Interscience Publishers, New York, **1964**.
[2] A. F. Wells, *Structural inorganic chemistry*, 6th ed., Oxford University Press, Oxford, UK, **1987**.
[3] W. A. Harrison, *Electronic structure and the properties of solids: the physics of the chemical bond*, Dover Publications, New York, **1989**.
[4] H. H. Kung, *Transition metal oxides: surface chemistry and catalysis*, Elsevier, Amsterdam, Netherlands, **1989**.
[5] V. E. Henrich, P. A. Cox, *The Surface Science of Metal Oxides*, Cambridge University Press, Cambridge, UK, **1994**.
[6] C. Noguera, *Physics and chemistry at oxide surfaces*, Cambridge University Press, **1996**.
[7] J. P. Colinge, K. Hashimoto, T. Kamins, S. Y. Chiang, E. D. Liu, S. S. Peng, P. Rissman, *Ieee Electron Device Lett.* **1986**, *7*, 279.
[8] V. Srinivasan, J. W. Weidner, *J. Electrochem. Soc.* **1997**, *144*, L210.
[9] J. Watson, *Sens Actuators* **1984**, *5*, 29.
[10] B. Noheda, *Curr. Opin. Solid-State Mater. Sci.* **2002**, *6*, 27.
[11] K. Eguchi, T. Setoguchi, T. Inoue, H. Arai, *Solid State Ionics* **1992**, *52*, 165.
[12] C. C. Hsu, N. L. Wu, *J. Photochem. Photobiol. A* **2005**, *172*, 269.
[13] S. Lindroos, M. Leskela, *Int. J. Inorg. Mater.* **2000**, *2*, 197.
[14] D. Golberg, Y. Bando, K. Fushimi, M. Mitome, L. Bourgeois, C. C. Tang, *J. Phys. Chem. B* **2003**, *107*, 8726.
[15] K. Nakagawa, T. Nakata, R. Konaka, *J. Org. Chem.* **1962**, *27*, 1597.
[16] K. Nakagawa, T. Tsuji, *Chem. Pharm. Bull.* **1963**, *11*, 296.
[17] K. Nakagawa, J. Sugita, K. Igano, *Chem. Pharm. Bull.* **1964**, *12*, 403.
[18] K. Nakagawa, J. Sugita, H. Onoue, *Chem. Pharm. Bull.* **1964**, *12*, 1135.
[19] C. Pierlot, V. Nardello, J. Schrive, C. Mabille, J. Barbillat, B. Sombret, J. M. Aubry, *J. Org. Chem.* **2002**, *67*, 2418.
[20] C. G. Levi, J. Y. Yang, B. J. Dalgleish, F. W. Zok, A. G. Evans, *J. Am. Ceram. Soc.* **1998**, *81*, 2077.
[21] A. Nazeri, P. P. TrzaskomaPaulette, D. Bauer, *J. Sol-Gel Sci. Technol.* **1997**, *10*, 317.
[22] Z. R. Tian, W. Tong, J. Y. Wang, N. G. Duan, V. V. Krishnan, S. L. Suib, *Science* **1997**, *276*, 926.
[23] I. E. Wachs, *Catal. Today* **1996**, *27*, 437.
[24] G. C. Bond, S. F. Tahir, *Appl. Catal.* **1991**, *71*, 1.
[25] Z. L. Wang, *Annu. Rev. Phys. Chem.* **2004**, *55*, 159.
[26] M. Fernandez-Garcia, A. Martinez-Arias, J. C. Hanson, J. A. Rodriguez, *Chem. Rev.* **2004**, *104*, 4063.
[27] M. E. Franke, T. J. Koplin, U. Simon, *Small* **2006**, *2*, 36.
[28] F. Zhu, Z. X. Yang, W. M. Zhou, Y. F. Zhang, *Solid State Commun.* **2006**, *137*, 177.
[29] W. J. Lee, W. H. Smyrl, *Electrochem. Solid-State Lett.* **2005**, *8*, B7.
[30] K. Deshpande, A. Mukasyan, A. Varma, *Chem. Mater.* **2004**, *16*, 4896.
[31] H. Y. Dang, J. Wang, S. S. Fan, *Nanotechnology* **2003**, *14*, 738.
[32] M. Monge, M. L. Kahn, A. Maisonnat, B. Chaudret, *Angew. Chem.* **2003**, *115*, 5479; *Angew. Chem. Int. Ed.* **2003**, *42*, 5321.
[33] M. Froba, A. Reller, *Prog. Solid State Chem.* **1999**, *27*, 1.
[34] M. Kakihana, *J. Sol-Gel Sci. Technol.* **1996**, *6*, 7.
[35] P. Cousin, R. A. Ross, *Mater. Sci. Eng. A* **1990**, *130*, 119.
[36] J. Livage, M. Henry, C. Sanchez, *Prog. Solid State Chem.* **1988**, *18*, 259.
[37] M. Niederberger, G. Garnweitner, *Chem. Eur. J.* **2006**, *12*, 7282.
[38] O. Carp, *Rev. Roum. Chim.* **2001**, *46*, 1189.
[39] F. Demangeot, V. Paillard, P. M. Chassaing, C. Pages, M. L. Kahn, A. Maisonnat, B. Chaudret, *Appl. Phys. Lett.* **2006**, *88*.
[40] M. L. Kahn, M. Monge, V. Colliere, F. Senocq, A. Maisonnat, B. Chaudret, *Adv. Funct. Mater.* **2005**, *15*, 458.
[41] F. Rataboul, C. Nayral, M. J. Casanove, A. Maisonnat, B. Chaudret, *J. Organomet. Chem.* **2002**, *643*, 307.
[42] Z. P. Sun, L. Liu, L. Zhang, D. Z. Jia, *Nanotechnology* **2006**, *17*, 2266.
[43] H. L. Cao, X. F. Qian, Q. Gong, W. M. Du, X. D. Ma, Z. K. Zhu, *Nanotechnology* **2006**, *17*, 3632.
[44] T. Trindade, P. O'Brien, N. L. Pickett, *Chem. Mater.* **2001**, *13*, 3843.

[45] R. Rossetti, R. Hull, J. M. Gibson, L. E. Brus, *J. Chem. Phys.* **1985**, *82*, 552.
[46] R. Rossetti, J. L. Ellison, J. M. Gibson, L. E. Brus, *J. Chem. Phys.* **1984**, *80*, 4464.
[47] L. Chen, J. Xu, D. A. Tanner, J. D. Holmes, M. A. Morris, unpublished results.
[48] S. Poulston, P. M. Parlett, P. Stone, M. Bowker, *Surf. Interface Anal.* **1996**, *24*, 811.
[49] B. G. M. C. López, C. Algora, I. Rey-Stolle, M. Gabas, J. R. Ramos-Barrado, *Appl. Surf. Sci.* **2007**, *253*, 5062.
[50] S. J. Pearton, C. R. Abernathy, M. E. Overberg, G. T. Thaler, D. P. Norton, N. Theodoropoulou, A. F. Hebard, Y. D. Park, F. Ren, J. Kim, L. A. Boatner, *J. Appl. Phys.* **2003**, *93*, 1.
[51] L. Q. Jing, Y. C. Qu, B. Q. Wang, S. D. Li, B. J. Jiang, L. B. Yang, W. Fu, H. G. Fu, J. Z. Sun, *Sol. Energy Mater. Sol. Cells* **2006**, *90*, 1773.
[52] E. A. Meulenkamp, *J. Phys. Chem. B* **1998**, *102*, 5566.
[53] J. C. Dupin, D. Gonbeau, P. Vinatier, A. Levasseur, *Phys. Chem. Chem. Phys.* **2000**, *2*, 1319.
[54] D. R. Mullins, S. H. Overbury, D. R. Huntley, *Surf. Sci.* **1998**, *409*, 307.
[55] L. X. Yin, Y. Q. Wang, G. S. Pang, Y. Koltypin, A. Gedanken, *J. Colloid Interface Sci.* **2002**, *246*, 78.
[56] V. Kumar, S. K. Sharma, T. P. Sharma, V. Singh, *Optical Mater.* **1999**, *12*, 115.

Received: May 23, 2008
Published online: November 7, 2008